FULL PAPER

Authentic fault models and dispersive tsunami simulations for outer-rise normal earthquakes in the southern Kuril Trench

Toshitaka Baba[1*] , Tetsuo No[2], Koichiro Obana[2], Kentaro Imai[2], Naotaka Chikasada[3], Yuichiro Tanioka[4] and Shuichi Kodaira[2]

Abstract

The southern Kuril Trench is one of the most seismically active regions in the world. In this study, marine surveys and observations were performed to construct fault models for possible outer-rise earthquakes. Seismic and sea-floor bathymetric surveys indicated that the dip angle of the outer-rise fault was approximately 50°–80°, with a strike that was slightly oblique to the axis of the Kuril Trench. The maximum fault length was estimated to be ~ 260 km. Based on these findings, we proposed 17 fault models, with moment magnitudes ranging from 7.2 to 8.4. To numerically simulate tsunami, we solved two-dimensional dispersive wave and three-dimensional Euler equations using the outer-rise fault models. The results of both simulations yielded identical predictions for tsunami with short-wavelength components, resulting in significant dispersive deformations in the open ocean. We also found that tsunami generated by outer-rise earthquakes were affected by refraction and diffraction because of the source location beyond the trench axis. These findings can improve future predictions of tsunami hazards.

Keywords Outer-rise earthquake, Southern Kuril Trench, Dispersive tsunami, Three-dimensional tsunami simulation, Fault modeling
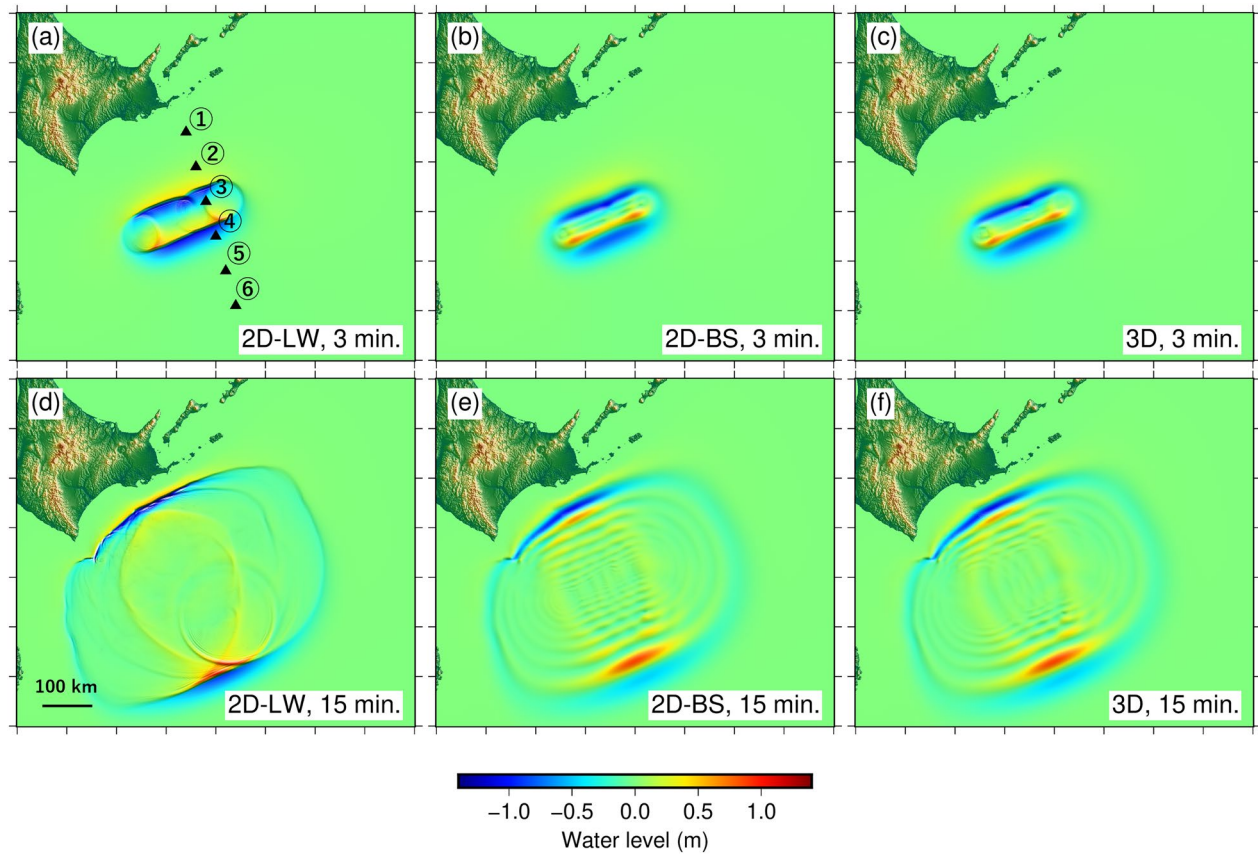
---

*Correspondence:
Toshitaka Baba
baba.toshi@tokushima-u.ac.jp
Full list of author information is available at the end of the article

Graphical Abstract

1 Introduction

The Pacific Plate subducts beneath the North American Plate (or Okhotsk Plate) at a rate of ~9 cm/year (Fig. 1a, Bird 2003) in the southern Kuril Trench off the coast of Hokkaido, Japan. Subduction has resulted in numerous earthquakes accompanied by tsunami. Based on past earthquakes, the Headquarters for Earthquake Research Promotion (2018) defined Tokachi-oki and Nemuro-oki as seismic segments of interest. In the Tokachi-oki segment, an interplate earthquake, called the 2003 Tokachi-oki earthquake, with a moment magnitude (M) of M8.0 occurred in 2003 (Kim et al. 2023; Tanioka et al. 2004a, b); this was a recurrence of the M8.2 earthquake that occurred in 1952 (Hamada et al. 2004; Satake et al. 2006), although the source region was slightly smaller in 2003. In the Nemuro-oki seismic segment, M8.3 and M7.8 interplate earthquakes occurred in 1894 and 1973, respectively (Tanioka et al. 2007; Nishimura 2009). Tsunami sediments and numerical studies have also indicated that the Tokachi-oki and Nemuro-oki segments ruptured simultaneously during a supergiant earthquake in the seventeenth century (Nanayama et al. 2003; Satake et al. 2005, 2008; Ioki and Tanioka 2016). Supergiant earthquakes recur at longer intervals than M8 inter-plate earthquakes, with recent examples including the 2004 Sumatra earthquake (Rubin et al. 2017) and the 2011 Tohoku earthquake (Namegaya and Satake 2014). Because the Nemuro-oki segment has not experienced interplate earthquakes exceeding M8 since 1894, there is a concern that a giant or supergiant interplate earthquake may occur. Additionally, intra-slab earthquakes are active in the region, including the 1993 Kushiro-oki earthquake (M7.6) (Takeo et al. 1993) and the 1994 earthquake off the east coast of Hokkaido (M8.4) (Tanioka et al. 1995; Tsuji et al. 1995).

Interplate earthquakes may have enhanced the seismic activity in the outer-rise region of the Kuril Trench. For example, the 1896 Meiji Sanriku earthquake (Tanioka and Satake 1996) was followed by the 1933 Showa Sanriku earthquake (Kanamori 1971; Abe 1978) in the Japan
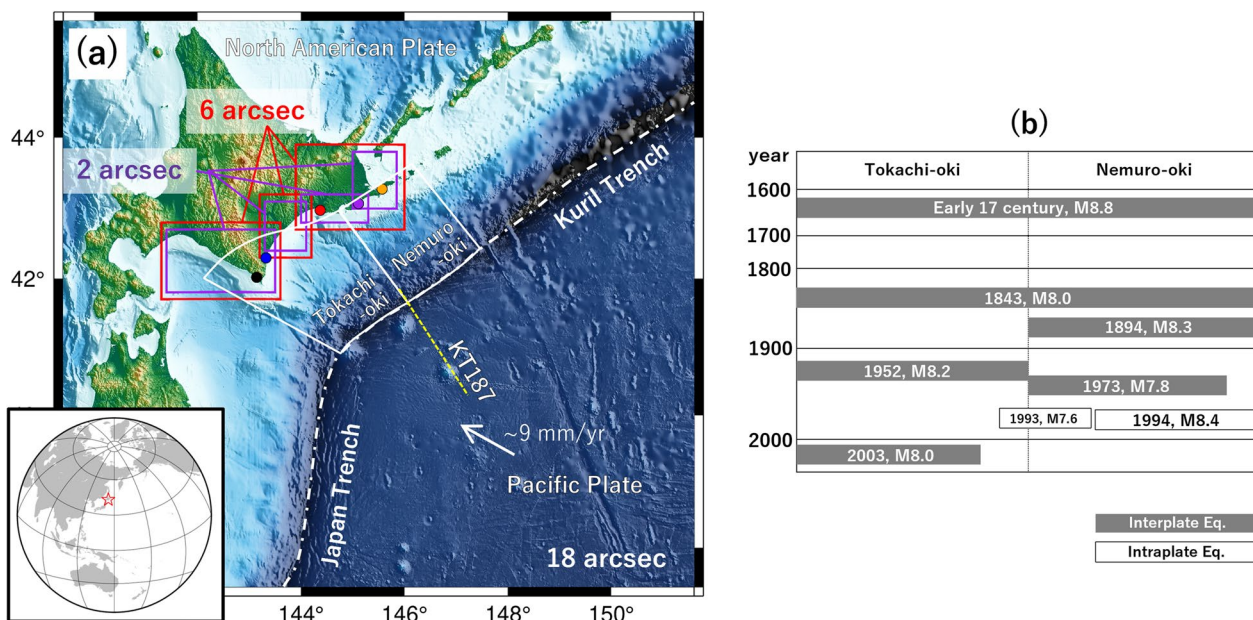
Fig. 1 a Tsunami calculation area. The computational grid interval is 18 arcsec in the mapped area. For the nested tsunami calculations (Sect. 2.2.3), we used 6-arcsec (red rectangles) and 2-arcsec (purple rectangles) interval grids. The yellow rectangle shows the 105R outer-rise fault, and the thick line is the top edge of the fault. The dotted line in light blue indicates the multichannel seismic reflection (MCS) survey line, KT187, shown in Fig. 2. Solid white lines surround the Tokachi-oki and Nemuro-oki seismic segments. The colored dots along the coast indicate output points of the calculated tsunami waveforms in Fig. 6 (orange: Nemuro–Hanasaki, purple: Kiritappu, red: Kushiro, blue: Tokachi, black: Erimo). **b** The timeline of large earthquakes in the Tokachi-oki and Nemuro-oki seismic segments

Trench adjacent to the southern Kuril Trench. The background seismicity of normal fault mechanisms also increased in the outer-rise region following the 2011 Tohoku earthquake (Asano et al. 2011). Other pairs of interplate and outer-rise earthquakes include the 2006 and 2007 Kuril earthquakes (Ammon et al. 2008; Fujii and Satake 2008; Baba et al. 2009; Lay et al. 2009) and the 2009 Samoa earthquake (Lay et al. 2010; Okal et al. 2010; Yokoi et al. 2023). In the latter, interplate and outer-rise earthquakes occurred almost simultaneously.

Compared to interplate earthquakes, research on outer-rise earthquakes remains limited. In recent years, we have conducted intensive surveys of outer-rise earthquakes in the Japan Trench to advance tsunami predictions (Obana et al. 2012, 2018, 2019; Fujie et al. 2016; Baba et al. 2020, 2021). Seismic surveys and observations have indicated that the dip angle of the outer-rise faults in the Japan Trench range from 45–75°, the upper edge of the faults almost reaches the seafloor, the thickness of the seismogenic layer is ~40 km, and the rigidity is approximately 65 GPa. Based on these findings, we proposed 33 outer-rise fault models and predicted tsunami based on these faults. We concluded that one of the 33 faults (No. 10) reproduced the coastal tsunami heights observed during the 1933 Showa-Sanriku earthquake (Baba et al. 2021). This tsunami prediction was a complete forward

model; therefore, the fact that one of the 33 faults reproduced the past tsunami ensured the suitability of our method for future predictions.

In this study, we used a procedure similar to that reported by Baba et al. (2021) to predict tsunami from outer-rise earthquakes in the southern Kuril Trench. Here, we describe our marine survey and propose 17 fault models for outer-rise earthquakes. We employed two- and three-dimensional (2D and 3D) methods to simulate tsunami and then compared an outer-rise tsunami with a tsunami from an interplate earthquake to understand the characteristics of outer-rise tsunami in the southern Kuril Trench. The results of this study will provide critical information for mitigating damages from future tsunami.

2 Data and methods
2.1 Outer-rise fault models in the southern Kuril Trench
2.1.1 Marine seismic surveys and bathymetric data compilation
We documented surveys of outer-rise normal faults along the southern Kuril Trench. Multi-channel seismic reflection (MCS) surveys were conducted to determine the geometry of the faults beneath the seafloor. The MCS surveys lasted from 2016 to 2020, for a total of 34 survey lines across four scientific cruises on research vessels of

Baba *et al. Earth, Planets and Space*   (2024) 76:98

Page 4 of 14

the Japan Agency for Marine–Earth Science and Technology (JAMSTEC) (Additional file 1: Fig. S1). The data obtained were processed for noise reduction in the time domain, and then transformed in the depth domain. Multiple reflections were removed using a surface-related multiple elimination method, radial trace deconvolution, and a high-resolution parabolic radon filter. Ghost reflection rejection further improved the amplitude reduction at the notch frequency and restored the amplitude of the low-frequency component. Figure 2 presents the MCS survey results obtained in in this study.

We estimated three fault parameters––fault throw, horizontal displacement, and dip angle––from the interpreted fault lines and the configuration of the upper surface of the oceanic crust. Horst-and-graben structures broke through the seafloor, corresponding to the shallow parts of the outer-rise faults. Both landward- and seaward-dipping faults were observed. The fault displacement estimated from the seafloor topography was lower than that estimated from the reflection surface on the oceanic crust, owing to new sedimentation, seafloor collapse, and erosion of the fault topography (e.g., Nakamura et al. 2013; Boston et al. 2014). Therefore, it was appropriate to estimate the fault configuration using the MCS survey results rather than the seafloor topography alone.

We created a digital elevation model (DEM) of the seafloor by compiling several existing datasets, including bathymetric grid data from Tohoku (Hydrographic and Oceanographic Department, Japan Coast Guard and JAMSTEC 2011) and the M7000 series bathymetric data (Japan Hydrographic Association 2009; 2012), along with General Bathymetric Chart of the Oceans (GEBCO) (GEBCO Compilation Group 2019; 2020), Shuttle Radar Topography Mission (SRTM15+) (Tozer et al. 2019), and JTOPO30v2 (Japan Hydrographic Association 2011) grid data. We used the JAMSTEC multibeam echosounder dataset as the base data because of its high precision and subsequently filled in gaps between the JAMSTEC dataset with the other publicly available datasets. The horizontal grid spacing in their compliant DEM was 0.0005° (~ 50 m) and the DEM was adequate for imaging the spatial connectivity of the outer-rise fault morphology. The spatial connectivity of the fault topography was comparable to that reported in previous studies (Kobayashi et al. 1998; Nakanishi 2011; Izumi et al. 2017). Therefore, in this study, we used this DEM data to determine the lengths and strike directions of the outer-rise fault models.

Based on the MCS results and DEM data, we identified 293 faults (hereafter referred to as unit faults), of which 148 and 145 were landward- and seaward-dipping, respectively (Fig. 3a). The mean strike of the faults mapped in this study was N67°E, with most oriented between N60°E and N75°E. The strikes of many unit faults were close, but slightly oblique, to those of the axis of the western Kuril Trench (N65°E) and the Mesozoic lineation of geomagnetic anomalies (N70°E, Nakanishi 2011). Most unit faults had dip angles of 65°–75°.

2.1.2 Earthquake observations

Microseismic observations utilizing 34 pop-up ocean bottom seismographs and 13 S-Net cable-connected seismographs (Aoi et al. 2019) were performed from April to June of 2022. We obtained hypocenter locations for 390 earthquakes of which were estimated with location errors of less than 5 km (Fig. 4). The largest event was M3.4 and the lower detection limit was approximately M1.0. Most
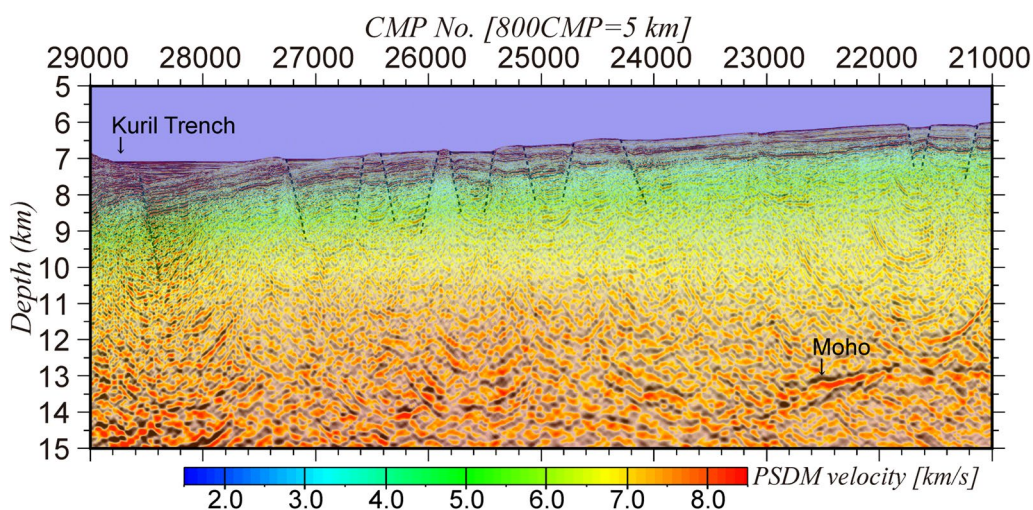

Fig. 2 MCS survey results with stratigraphic and fault interpretations of KT187 (Fig. 1)

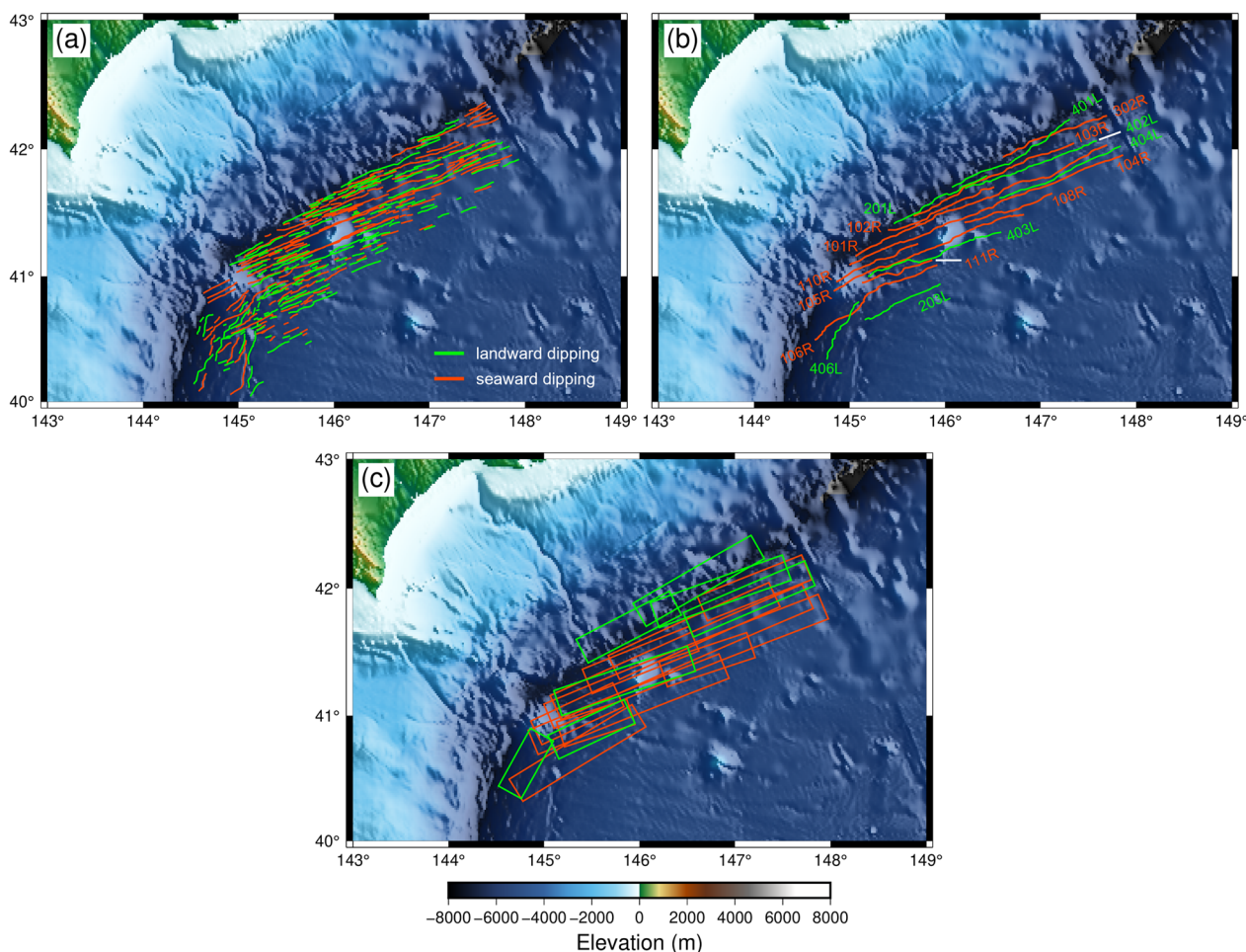Baba *et al. Earth, Planets and Space* (2024) 76:98

Page 5 of 14

Fig. 3 a Seafloor trace of the unit faults identified in this study. Green and red lines indicate landward- and seaward-dipping faults, respectively. **b** Seafloor trace of the outer-rise faults connected the unit faults within 5 km of each other and dipping in the same direction (landward or seaward). **c** Proposed outer-rise earthquake faults approximated by rectangular shape. Fault parameters are shown in Table 1

earthquakes occurred at depths ≤ 30 km below sea level and within ~ 100 km of the Kuril Trench axis. Seismicity was aligned along the horst-and-graben structures parallel to the Kuril Trench axis. In addition, other seismic swarms were observed parallel to the Japan Trench and in a northwest-southeast direction around the junction of the Kuril and Japan Trenches. Therefore, we speculated complex deformations in the subducting plate. Focal mechanism solutions were obtained for 10 earthquakes, which indicated normal faulting with the T-axis almost perpendicular to the trench axis. The dip angle of the steepest nodal plane of the focal mechanism ranged from ~ 50°–80°, with a mean of 57°. In associated observations in the Japan Trench (Obana et al. 2021, 2018), earthquakes with normal fault mechanisms occurred at depths of ~ 50 km. The bottom of the normal fault earthquakes that occurred in the southern Kuril Trench may have been somewhat shallower than those in the

Japan Trench. However, because of the short observation period, we cannot conclude that normal-fault earthquakes did not occur at depths > 30 km in the southern Kuril Trench. Moreover, the stress field in the subducting Pacific Plate within the Japan Trench changed such that normal fault earthquakes at greater depths became more common because of the Tohoku earthquake (Kubota et al. 2019). Thus, the seismogenic thickness at which outer-rise normal fault earthquakes occur in the southern Kuril Trench remains uncertain.

2.1.3 Outer-rise fault models

Source fault models for large outer-rise earthquakes were constructed from the unit faults using the method of Matsuda (1990) and by referring to a simulation study of tsunami generated by normal faults in the subducting plate of the Japan Trench (Baba et al. 2020). We connected the unit faults within 5 km of each other and
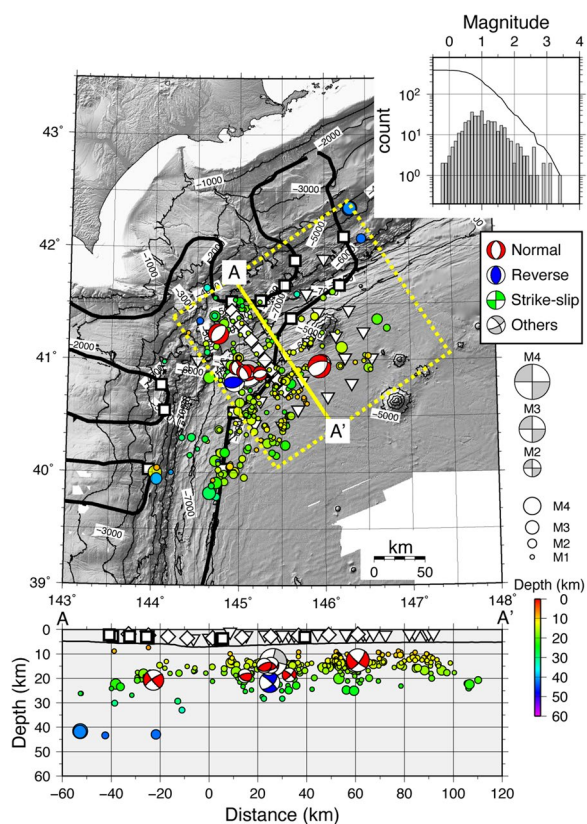
Baba *et al. Earth, Planets and Space*   (2024) 76:98

Page 6 of 14

Fig. 4 Hypocentral distribution and focal mechanisms determined by ocean-bottom seismic observations. The upper right graph shows the magnitude-frequency distribution using the earthquakes shown on the map. Earthquakes in the yellow dotted rectangle were projected on the cross-section along A–A' in the figure below

dipping in the same direction (landward or seaward; Fig. 3b). Those with a connected fault length > 60 km were assumed to be the source faults. Although the source faults were along curved traces on the seafloor, we approximated each fault using a rectangle for simplicity (Fig. 3c). Here, rectangular faults are referred to as faults. As we connected the unit faults identified from the seafloor topographic survey (Fig. 3a), the strike of the faults was approximately along the trench axis. Although our seafloor seismic observations identified seismic activity non-parallel to the axis around the junction of the Kuril and Japan Trenches, we could not constrain fault models for them because the hypocentral distribution was sparse. However, this is not of concern because the length of the seismic activity was too short to generate a damaging tsunami. The length (L) of the maximum fault was estimated as ~260 km. The dip angle was set at 60° by referring to the angles of the shallow part of the fault (65°–75°) revealed by the MCS surveys and those obtained from the higher nodal plane of the fault mechanism solutions of the outer-rise earthquakes (50°–80°). The thickness of

the seismogenic layer of outer-rise earthquakes in this area remains unknown. Therefore, we used a thickness of 40 km from the Japan Trench (Baba et al. 2020). The fault width (W) was constrained by the thickness of the seismogenic layer (i.e., 46.2 km). The amount of slip was calculated from L using an earthquake scaling method developed for outer-rise earthquakes (Álvarez-Gómez et al. 2012). In this way, we proposed 17 outer-rise fault models ranging from M7.2 to M8.4 (Table 1).

2.2 Tsunami models
2.2.1 Three-dimensional model
Two-dimensional long-wave models are standard when simulating tsunami propagation because the wavelength of a tsunami is sufficiently longer than the water depth. However, we speculate that more than one long-wave model is required for calculating tsunami generated by outer-rise earthquakes with short fault widths and steep dip angles under the deep sea. The long-wave model stems from the application of long-wave approximation to a 3D Euler's equation. To clarify the characteristics of outer-rise tsunami, we calculated those generated by outer-rise earthquakes by solving Euler's equation in a 3D finite volume scheme. We used the open-source non-hydrostatic wave model (NHWAVE v. 2.0) software (Ma et al. 2012, 2013, 2015; Kirby et al. 2016), which simulates tsunami. NHWAVE is frequently used to simulate short-wavelength tsunami caused by submarine landslides or volcanic collapses (Ma et al. 2012, 2013, 2015; Kirby et al. 2016; Grilli et al. 2019) and is appropriate for calculating outer-rise earthquake tsunami, although 3D models are more computationally demanding than 2D models. Here, we focused on the generation and initial stages of tsunami propagation. We assumed an incompressible fluid for the 3D simulations. We also neglected the viscous term because the generation and initial stages of tsunami propagation are deep-sea processes in which the effect of viscosity can be small.

Figure 1a shows the area calculated for the 3D tsunami simulation. We used the Global tsunami Terrain Model (GtTM, Chikasada 2020) for bathymetry data and down-sampled it at 500-m intervals in the east and north. The vertical grid interval varied depending on the water depth and number of layers in NHWAVE. The number of vertical layers was set to three. Simulations were repeated by varying the number of vertical layers and the results were identical for three or more layers. We calculated the vertical crustal deformation on the seafloor derived from the 105R fault (see Table 1) using an analytical solution for the deformation of a semi-infinite homogeneous elastic body (Okada 1985). In the 3D tsunami simulations, we generated the vertical deformation at the bottom of the seawater layer with a rise time of 30 s. The time step

Table 1 Parameters of the 17 proposed outer-rise fault models

ID	Lat. (°)	Lon. (°)	Depth (km)	Length (km)	Width (km)	Dip (°)	Strike (°)	Rake (°)	Slip (m)	Magnitude (M)
101R	41.15715	145.0645	0.1	239.9	46.2	60.0	65.2	270.0	6.7	8.4
102R	41.36635	145.4015	0.1	100.1	46.2	60.0	67.7	270.0	1.3	7.7
103R	41.4745	145.6732	0.1	153.2	46.2	60.0	64.9	270.0	2.9	8.0
104R	41.09004	144.998	0.1	257.7	46.2	60.0	67.2	270.0	7.6	8.4
105R	40.88314	144.8342	0.1	180.1	46.2	60.0	67.5	270.0	3.9	8.2
106R	40.49308	144.6352	0.1	126.9	46.2	60.0	58.2	270.0	2.1	7.9
108R	41.42426	146.2039	0.1	80.7	46.2	60.0	71.2	270.0	0.9	7.5
110R	40.95623	144.8612	0.1	79.3	46.2	60.0	64.6	270.0	0.9	7.5
111R	40.94887	145.1301	0.1	64.9	46.2	60.0	71.9	270.0	0.6	7.3
201L	41.79338	146.4395	0.1	91.5	46.2	60.0	243.0	270.0	1.1	7.6
203L	40.93924	145.9527	0.1	74.1	46.2	60.0	245.0	270.0	0.8	7.4
302R	41.93895	146.6063	0.1	96.9	46.2	60.0	67.9	270.0	1.3	7.6
401L	42.23355	147.3071	0.1	118.1	46.2	60.0	240.5	270.0	1.8	7.8
402L	42.06479	147.5879	0.1	121.6	46.2	60.0	250.6	270.0	1.9	7.8
403L	41.35092	146.5868	0.1	123.4	46.2	60.0	252.1	270.0	2.0	7.8
404L	42.02392	147.8378	0.1	114.6	46.2	60.0	247.3	270.0	1.7	7.8
406L	40.79756	145.0978	0.1	58.5	46.2	60.0	209.2	270.0	0.5	7.2

Fault origin (latitude, longitude, and depth) is the closer corner of the upper edge of the fault plane assuming that the fault dips to the right facing the strike direction. Rake angle is measured in counterclockwise from the strike direction

width was set to 0.1 s to ensure stability and the integral time was 60 min to focus on the generation and initial stage of tsunami propagation and save computational resources.

2.2.2 Single-grid two-dimensional model
Two-dimensional dispersive wave models provide another means of calculating short-wavelength tsunami (Peregrine 1972; Saito 2019). While dispersive wave models can also approximate Euler's equation, they are less accurate. However, they can handle tsunami with shorter wavelengths than the long-wave equation. Dispersive wave models have been used in numerous previous studies to compute tsunami caused by outer-rise earthquakes because they may be easily connected to tsunami run-up calculations (Tanioka et al. 2018; Baba et al. 2020, 2021). To the best of our knowledge, a 2D dispersive model has never been compared with a 3D model for outer-rise earthquake tsunami, which has been accomplished here.

In this study, we used our open-source software, JAG-URS (Baba et al. 2015, 2017), to construct a 2D dispersive wave model. JAGURS is an in-team development code that is parallelized using a message-passing interface and open multi-processing techniques. It can efficiently improve spatial resolution using a nested grid algorithm and is available on personal computers, cluster machines, and supercomputers. We used JAGURS to calculate tsunami by solving a nonlinear dispersive wave equation that included an advection term. However, for comparison with the 3D model, we neglected the viscous effects (i.e., bottom friction) in the simulations. The computational conditions were identical to those of the 3D model except for the tsunami input. Figure 1a shows the computational domain with a grid interval of 500 m in the east and north. The time step width was set to 0.1 s. Okada's (1985) method was used to calculate the vertical displacement of the seafloor from the 105R fault. This deformation was then applied to the sea surface with a rise time of 30 s after applying the hydraulic filter of Kajiura (1963), which included the non-hydrostatic effect on tsunami generation. The 60 min propagation was solved using a 2D dispersive wave model. For comparison, tsunamis were calculated using a nonlinear long-wave model. The calculated vertical seafloor deformation was directly applied to the sea surface with a rise time of 30 s without Kajiura's (1963) filter. The 60 min propagation was solved using a 2D nonlinear long-wave model provided by JAGURS. Both the dispersion and Kajiura's hydraulic filter are due to the non-hydrostatic effects of the fluid; therefore, this model could be described as a tsunami model without non-hydrostatic effects.

2.2.3 Nested grid two-dimensional model
Following the setup and comparison of our 3D and 2D tsunami models, we aimed to predict coastal tsunami heights from outer-rise earthquakes. We used nonlinear dispersive wave equations similar to those used in Sect. 2.2.2. However, bottom friction terms and nested

Baba *et al. Earth, Planets and Space*   (2024) 76:98

Page 8 of 14

grid algorithms were used to calculate tsunami near land and during run-ups. The nested grids consisted of domains at grid intervals of 18–6-2 arcsec and were focused on southeastern Hokkaido. We resampled GtTM topographic data to create finer grid domains (Fig. 1a) and we did not oversample finer than the resolution of the original data (GtTM was gridded by 2 arcsec intervals). The tsunami generation method was the same as that described in Sect. 2.2.2. We calculated vertical crustal deformation at the seafloor using the analytical solution of Okada (1985) and input this deformation after filtering using Kajiura's (1963) method to the sea surface with a rise time of 30 s. The time step width was 0.1 s, and the integral time was 6 h to capture the entire tsunami process along the coast.

3 Tsunami simulation results

Figure 5 shows the results of the outer-rise tsunami calculated based on Euler's equation (see Sect. 2.2.1), nonlinear dispersive wave equation, and nonlinear long-wave equation (see Sect. 2.2.2). Figure 6 shows a comparison of the calculated tsunami waveforms at the locations
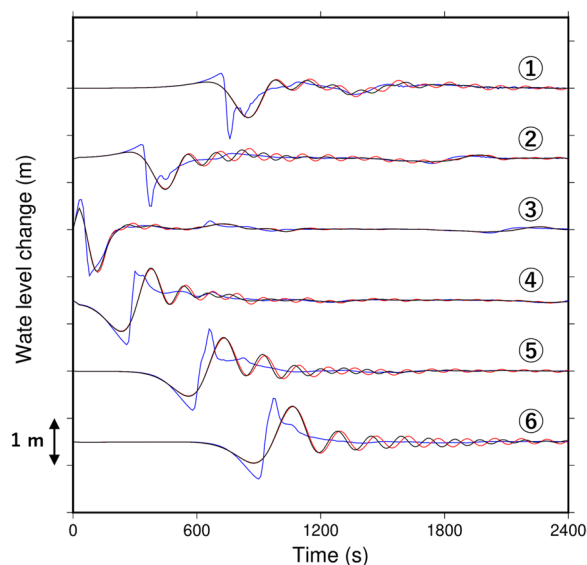

Fig. 6 Tsunami waveforms calculated at the locations shown in Fig. 3a. Blue lines were obtained from the nonlinear long-wave equation, red lines from the nonlinear dispersive wave equation, and black lines from Euler's equation
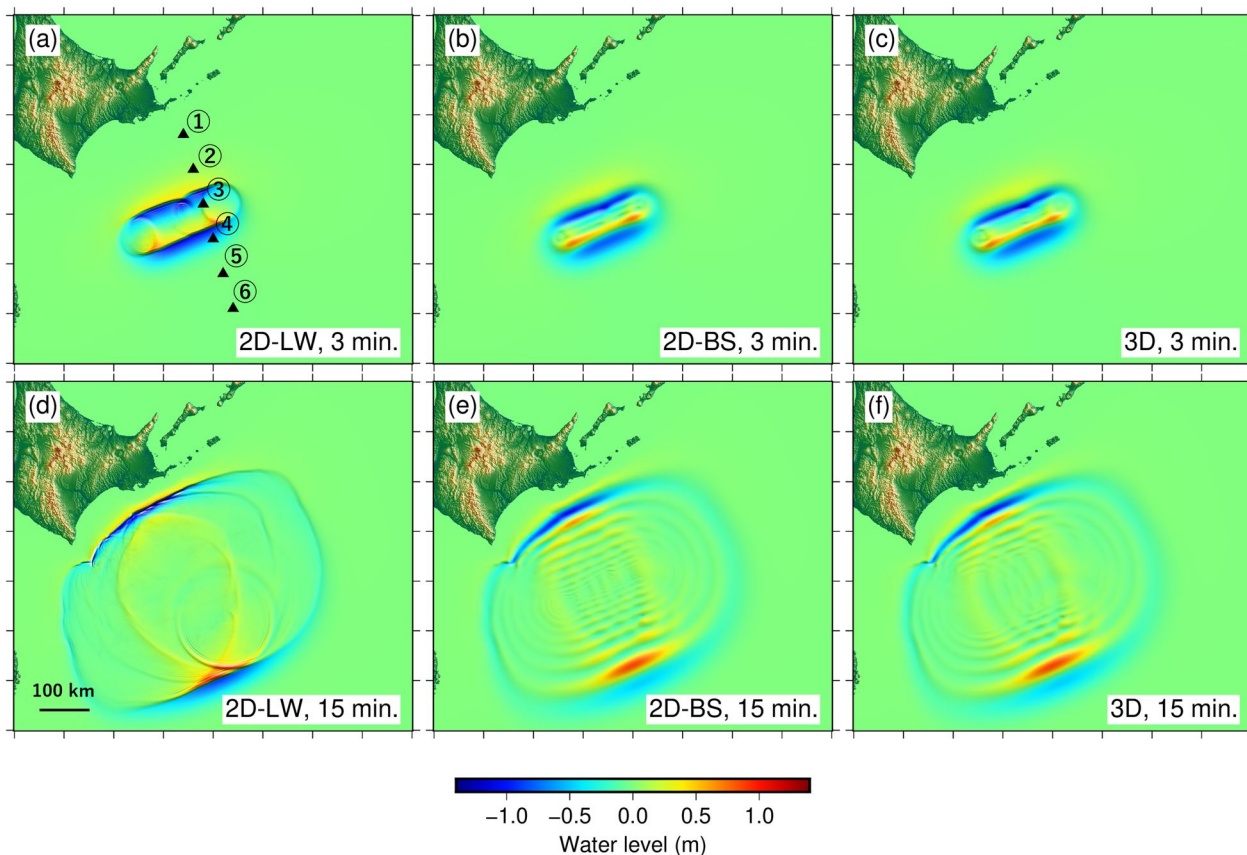

Fig. 5 Tsunami calculations for the 105R outer-rise fault using **a**, **d** the nonlinear long-wave equation (2D-LW), **b**, **e** nonlinear dispersive wave equation (2D-BS), and **c**, **f** Euler's equation (3D). The solutions of the nonlinear dispersive wave equation and the Euler's equation are consistent

indicated by the triangles in Fig. 5a. This comparison indicates that the waveforms calculated using the nonlinear dispersive wave equation were consistent with those obtained from Euler's equations in terms of the maximum amplitude, dominant frequency, and formation of wave trains by dispersion. However, the waveforms obtained from the nonlinear long-wave model differed from those obtained from the other two tsunami models. The nonlinear long-wave model did not generate dispersive wave trains and predicted the trough-to-crest amplitude of the first wave to be larger than that of the other models. The shape of the first wave also changed sharply.

Small but noticeable differences were observed in the dispersive waves between the 3D Euler's and the 2D dispersive wave models (Figs. 5 and 6). The 2D dispersive wave model delayed the later dispersive wave trains and caused weak amplitude decay. This difference was also seen in previous studies involving tsunami calculations for interplate earthquakes (Oishi et al. 2013) and for a volcanic tsunami (Sandanbata et al. 2021). This is a known limitation of 2D dispersive models. The phase velocity in the 2D dispersive model used in this study was slower than that in the analytical solution of water waves for waves with extremely short wavelengths. The limitations of 2D dispersive models should be examined for detailed analyses of source processes in outer-rise earthquakes. Nevertheless, the 2D dispersive model was sufficient to estimate tsunami damages because it reproduced the maximum amplitude and dominant frequency of the tsunami.

In this study, we predicted coastal tsunami of the 105R fault using the 2D dispersive model with nested grids, as described in Sect. 2.2.3 (Fig. 7a, c). A maximum tsunami height of ~ 8 m occurred at ~ 144.8°E on the coast of Hokkaido and another tsunami peak ~ 7 m was observed at ~ 143.2°E near Cape Erimo. Figure 8a shows the
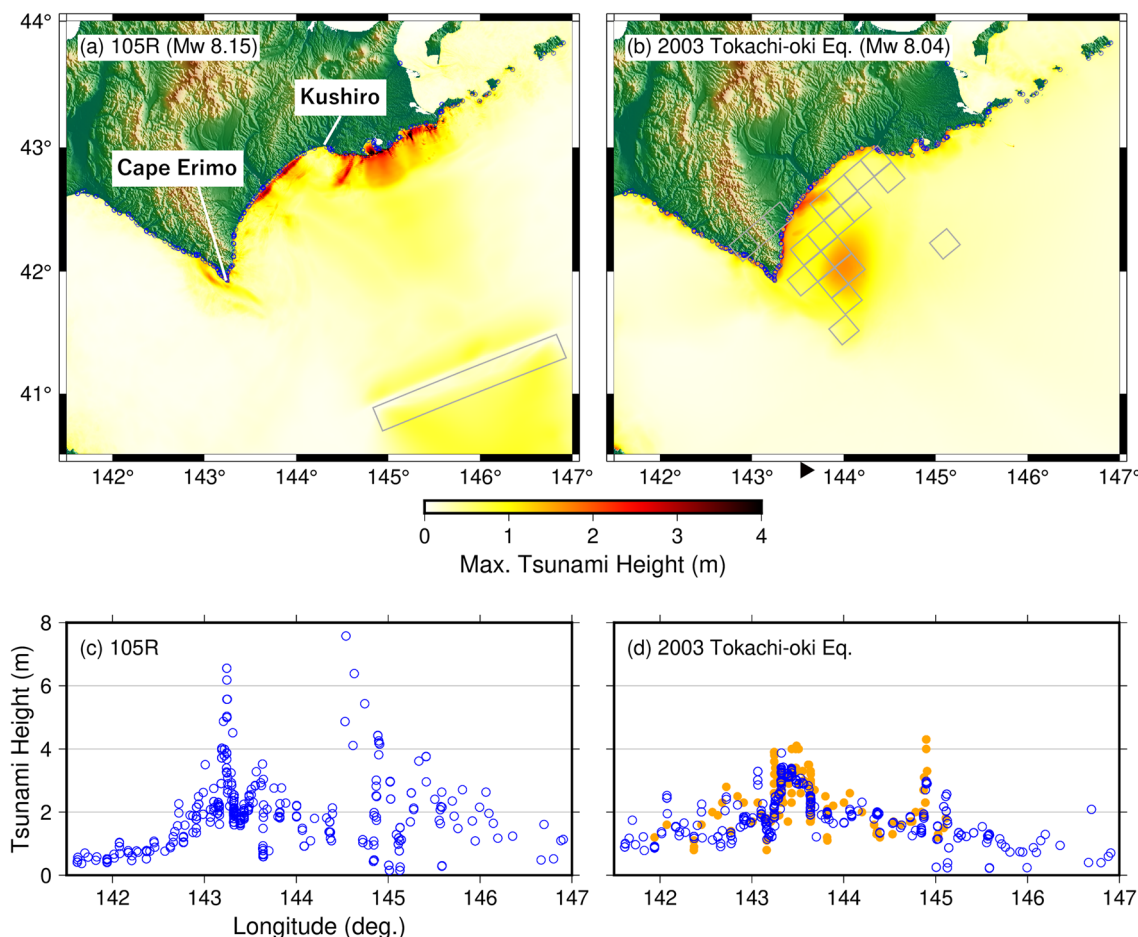

Fig. 7 Tsunami simulated by the two-dimensional nonlinear dispersive wave equation; from **a**, **c** 105R and **b**, **c** the 2003 Tokachi-oki earthquake. **a**, **b** Maximum tsunami height distributions. The gray rectangle and squares indicate source areas with slip larger than 1 m. **c**, **d** Plots of the tsunami heights at the coast. Blue and orange circles denote calculated and observed values (Tohoku University and Japan Nuclear Energy Safety Organization 2010), respectively
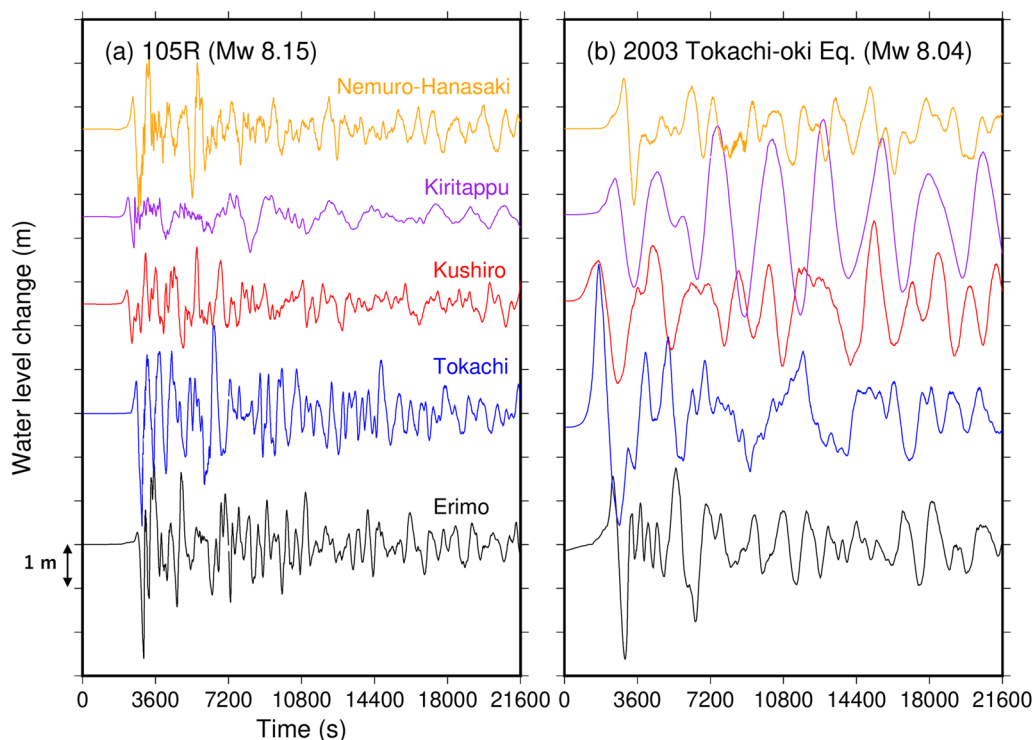
Fig. 8 Comparisons of calculated tsunami waveforms at the output points shown in Fig. 1

tsunami waveforms calculated at the imaginary observation points shown in Fig. 1a. The power spectral densities (Additional file 1: Fig. S2) indicated that the dominant frequency at the Nemuro–Hanasaki station (orange point in Fig. 1a) was approximately 0.0015 Hz (10 min). Additional file 1: Figs. S3–S18 show the maximum tsunami height distributions calculated using the other fault models listed in Table 1. An aggregated map of the maximum tsunami height for the 17 outer-rise faults (Additional file 1: Fig. S19) is similar to the tsunami calculation result for the largest earthquake of M8.4 (104R, Additional file 1: Fig. S6). Therefore, the 104R model should be used for a deterministic tsunami hazard assessment of the outer-rise earthquakes in this region.

We assumed that the strike of the faults was well constrained by the horst-and-graben topography and the MCS surveys. The dip of the fault was fixed at 60° for simplicity, while the marine surveys indicated that the dip angle of the outer-rise faults was approximately 50°–80°. Similarly, we assumed pure normal fault slip (270°) for all the fault models. Our previous study (Baba et al. 2020) investigated uncertainties in tsunami predictions related to the fault parameters using numerical tsunami simulations that changed the dip and rake angle by ± 15°. Predicted tsunami heights at the coast changed by up to 10% for varying dip angles and about 2% for varying rake angles. We suspect equivalent uncertainties in tsunami

prediction for the outer-rise earthquakes in the Kuril Trench.

4 Discussion
4.1 Comparison with tsunami caused by an interplate earthquake

The 2003 Tokachi-oki earthquake was an M8.0 interplate earthquake accompanied by a tsunami. Tide gauges were used to record the tsunami waveforms and post-tsunami surveys measured the height of tsunami evidence along the coast. We compared the tsunami generated by the 2003 Tokachi-oki earthquake and an outer-rise earthquake (105R) to understand the characteristics of tsunami generated by outer-rise earthquakes. The tsunami caused by the 2003 Tokachi-oki earthquake were simulated using the method described in Sect. 2.2.3 but with the fault model excluded. A fault model of this earthquake was developed by Kim et al. (2023), who explained the tsunami waveforms observed by seafloor pressure gauges. Figure 5b, d compares the calculated tsunami heights and the observed heights of the post-tsunami survey. Aida's (1978) reproduction indices, K and κ, were obtained as 1.01 and 1.31, respectively, indicating good agreements between the observed and simulated tsunami, thus validating our method.

A comparison of the tsunami heights along the coast of the 2003 Tokachi-oki earthquake with the outer-rise fault

Baba *et al. Earth, Planets and Space*   (2024) 76:98

Page 11 of 14

model of 105R showed that height localization was significant at 105R (Fig. 5c). This difference was evident near Cape Erimo, at ~ 143.2°E. Outer-rise earthquake faults occurred seaward of the trench axis; therefore, they were affected by the seafloor topography (i.e., refraction and diffraction). Generally, the energy of a tsunami is concentrated at the landward edge that protrudes into the sea. A large outer-rise tsunami near Cape Erimo was affected by diffraction. However, the tsunami caused by the Tokachi-oki earthquake, which was located near the coast, arrived before the effects of refraction and diffraction strengthened. Another difference in the tsunami height was observed east of Kushiro. As this area is oriented in the dip direction of the outer-rise fault, the tsunami arrived directly from the source. This caused tsunami directivity, in which a large amount of energy from a tsunami generally radiates toward the dip direction of earthquake faults. However, the tsunami caused by the 2003 Tokachi-oki earthquake arrived non-directly in this area. Additionally, we observed a difference in the dominant frequency of the tsunami waveforms (Fig. 6) and the power spectral density (Additional file 1: Fig. S2). The power spectral density at Nemuro–Hanasaki indicated that the dominant frequency of the 2003 Tokachi-oki tsunami waveform was 0.0006 Hz (28 min), which was clearly lower than the previously calculated 0.0015 Hz (10 min) of the outer-rise tsunami. Different frequency periods (wavelengths) can cause different responses in bays, which may result in unexpectedly large tsunami.

4.2 Tsunami calculations with variable fault widths

We constructed outer-rise fault models using bathymetric surveys, marine seismic observations, and MCS surveys, which allowed us to constrain the locations, dips, and depths of the upper edges of the faults. However, the lower edges of the faults (or thickness of the seismogenic layer) remain ambiguous. During the observation period, no earthquakes with normal fault mechanisms occurred in the southern Kuril Trench at depths > 30 km below sea level. We are still determining whether this is representative of the frequency of such earthquakes or an artefact of the short observation period. In adjustment studies of the Japan Trench (Obana et al. 2018), normal fault earthquakes occurred 50 km below sea level (with a seismogenic layer thickness of ~ 40 km). Therefore, based on tsunami prediction standards, the thickness of the seismogenic layer for outer-rise earthquakes along the southern Kuril Trench was equated to that of the Japan Trench. If the seismogenic layer is thinner than 40 km (i.e., the fault width is short), an outer-rise earthquake will excite a shorter-wavelength seafloor deformation with larger amplitude, assuming the equivalent earthquake magnitude.

We performed 3D tsunami calculations for different fault widths (black lines in Fig. 9). The amount of slip changed according to the fault width because the earthquake magnitude was constant. Contrary to our expectations, the tsunami waveforms in the first cycles computed for different fault widths were comparable. While the shape of the long-wavelength seafloor crustal deformation can be treated as identical to the shape of the initial water level of the tsunami, for the short-wavelength seafloor crustal deformation excited by a narrow outer-rise fault, the deformation at the seafloor becomes spatially smooth at the sea surface by a smoothing effect of the water column. We interpreted the consistency between the tsunami waveforms irrespective of the fault width as a consequence of superimposing changes in wavelength and amplitude of seafloor crustal deformation and the smoothing effect. However, the second wave appears sensitive to the fault width because their amplitudes clearly differ (arrows in Fig. 9). Therefore, the second tsunami wave should be used to estimate the fault width of outer-rise earthquakes.

The 3D model naturally considers the smoothing effect by solving the governing equations. However, because the 2D model did not automatically consider the effect, we applied the analytical smoothing filter by Kajiura (1963) to obtain the sea surface deformation and calculate the tsunami (red lines in Fig. 9). The maximum amplitudes of the first wave in the 2D calculations were almost the same as those of the tsunamis calculated by the 3D model, regardless of the fault width. The period
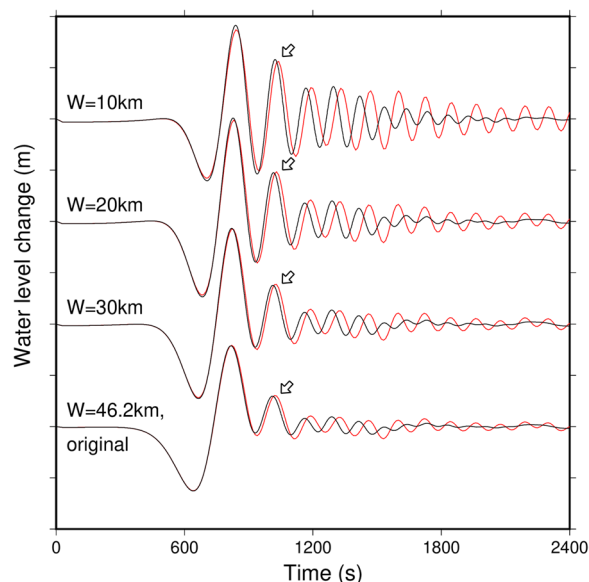

Fig. 9 Tsunami waveforms at point 5 in Fig. 3a calculated by changing the fault width (W) in the 2D nonlinear dispersive wave model (red) and 3D Euler's equation (black)

Baba *et al. Earth, Planets and Space*   (2024) 76:98

Page 12 of 14

of the tsunami was also comparable. However, the phase speed of the subsequent wave (dispersive wave) was slightly slower than that of the 3D model. In addition, the decay of the amplitude of the subsequent wave was relatively weak. This difference from the 3D model indicates the application limit of the 2D model used in this study. In conclusion, the 2D tsunami model is acceptable for predicting the maximum amplitude, which is essential for tsunami hazard assessment. On the other hand, the 3D tsunami model is preferable to use for detailed clarification of the rupture processes of outer-rise earthquakes.

5 Conclusions

In this study, we compiled bathymetric surveys, marine seismic observations, and MCS surveys along the southern Kuril Trench, and proposed 17 models of outer-rise faults that could rupture. Tsunami were predicted from the proposed faults using 2D and 3D computational models. The conclusions are as follows:

1. The dip angle of the outer-rise faults in this region ranged from 50° to 80° and strike was slightly oblique to the trench axis.
2. The length of the longest fault was 260 km, corresponding to a magnitude of M8.4.
3. The predictions of the 2D dispersive and 3D tsunami models were almost identical. Considering its ease of use, 2D dispersive models are suitable for predicting outer-rise tsunami.
4. Because outer-rise earthquakes occur far from land, tsunami generated by these earthquakes are more sensitive to the effects of refraction and diffraction owing to seafloor topography.
5. Outer-rise tsunami contain relatively high-frequency components due to the short width and high dip of the generative faults.

Our next challenge is to predict the detailed deformation of outer-rise tsunami near the coast and in bays using high-resolution topographic data. In this study, we used nonlinear dispersion and precise computational models. However, the 2-arcsec (~ 50-m) spatial resolution of the computational grid of was insufficient for reproducing the short-wavelength soliton-splitting waves that may have occurred near the coast. Soliton splitting increases the height of tsunami, so it should be included in models for disaster prevention, as should the amplification of tsunami caused by oscillations induced in bays. A grid resolution of ≤ 5 m is required to evaluate these factors. Similarly, the 3D effect is not negligible for detailed modeling of tsunami overtopping dikes and violent flows around buildings (Arikawa and Tomita 2016; Prabu et al. 2022). Because our

computational resources were limited, in future studies we will continue to work on high-resolution computations that can aid to mitigate disasters caused by outer-rise tsunami.

Abbreviations

DEM	Digital elevation model
GEBCO	General Bathymetric Chart of the Oceans
GtTM	Global tsunami terrain model
JAMSTEC	Japan Agency for Marine–Earth Science and Technology
M	Moment magnitude
MCS	Multichannel seismic reflection
NHWAVE	Non-hydrostatic wave
SRTM	Shuttle Radar Topography Mission

Supplementary Information

The online version contains supplementary material available at https://doi.org/10.1186/s40623-024-02046-z.

> Additional file 1.

Author contributions

T.B. performed the majority of the tsunami simulations and wrote the manuscript. T.N., K.O., and S.K. conducted marine topographic and seismic surveys. K.I., N.C., and Y.T. contributed to the discussion on tsunami modeling.

Availability of data and materials

We used the tsunami software JAGURS (Baba et al. 2015, 2017) provided in an online repository at http://dx.doi.org/https://doi.org/10.5281/zenodo.3737816 and NHWAVE (Ma et al. 2012, 2013, 2015; Kirby et al. 2016), available at https://github.com/JimKirby/NHWAVE. The Japan tsunami trace database is available at https://tsunami-db.irides.tohoku.ac.jp/tsunami/?LANG=-2 and was last accessed on 1 February 2024. JTOPO30v2 (Japan Hydrographic Association 2011) can be found at http://www.mirc.jha.jp/products/JTOPO30v2/. SRTM15+ (Tozer et al. 2019) is available at https://www2.jpl.nasa.gov/srtm/. GtTM (Chikasada 2020) is available at https://kiyuu.bosai.go.jp/GtTM/.

Declarations

Ethics approval and consent to participate

Not applicable.

Consent for publication

Not applicable.

Competing interests

The authors declare that they have no competing interests.

Author details

[1]Graduate School for Social and Industrial Science and Technology, Tokushima University, 2-1 Minami-Jyosanjima-Cho, Tokushima 770-8506, Japan. [2]Research Institute for Marine Geodynamics, Japan Agency for Marine-Earth Science

Baba *et al. Earth, Planets and Space*   (2024) 76:98

Page 13 of 14

and Technology, Yokohama, Japan. [3]National Research Institute for Earth Science and Disaster Resilience, Ibaraki, Japan. [4]Hokkaido University, Hokkaido, Japan.

References

Abe K (1978) A dislocation model of the 1933 Sanriku earthquake consistent with the tsunami waves. J Phys Earth 26(4):381–396. https://doi.org/10.4294/jpe1952.26.381

Aida I (1978) Reliability of a tsunami source model derived from fault parameters. J Phys Earth 26:57–73. https://doi.org/10.4294/jpe1952.26.57

Álvarez-Gómez JA, Gutiérrez Gutiérrez OQ, Aniel-Quiroga Í, González M (2012) Tsunamigenic potential of outer-rise normal faults at the Middle America trench in Central America. Tectonophysics 574–575:133–143. https://doi.org/10.1016/j.tecto.2012.08.014

Ammon CJ, Kanamori H, Lay T (2008) A great earthquake doublet and seismic stress transfer cycle in the central Kuril Islands. Nature 451(7178):561–565. https://doi.org/10.1038/nature06521

Aoi S, Suzuki W, Chikasada N, Miyoshi T, Arikawa T, Seki K (2019) Development and utilization of real-time tsunami inundation forecast system using S-net data. J Disaster Res 14(2):212–224. https://doi.org/10.20965/jdr.2019.p0212

Asano Y, Saito T, Ito Y, Shiomi K, Hirose H, Matsumoto T, Aoi S, Hori S, Sekiguchi S (2011) Spatial distribution and focal mechanisms of aftershocks of the 2011 off the Pacific coast of Tohoku Earthquake. Earth Planets Space 63(7):669–673. https://doi.org/10.5047/eps.2011.06.016

Arikawa T (2016) Tomita T (2016) Development of high precision tsunami runup calculation method based on a hierarchical simulation. J Disaster Res 11(4):639–646. https://doi.org/10.20965/jdr.2016.p0639

Baba T, Allgeyer S, Hossen J, Cummins PR, Tsushima H, Imai K, Yamashita K, Kato T (2017) Accurate numerical simulation of the far-field tsunami caused by the 2011 Tohoku earthquake, including the effects of Boussinesq dispersion, seawater density stratification, elastic loading, and gravitational potential change. Ocean Model 111:46–54. https://doi.org/10.1016/j.ocemod.2017.01.002

Baba T, Chikasada N, Imai K, Tanioka Y, Kodaira S (2021) Frequency dispersion amplifies tsunamis caused by outer-rise normal faults. Sci Rep 11(1):1–11. https://doi.org/10.1038/s41598-021-99536-x

Baba T, Chikasada N, Nakamura Y, Fujie G, Obana K, Miura S, Kodaira S (2020) Deep investigations of outer-rise tsunami characteristics using well-mapped normal faults along the Japan trench. J Geophys Res: Solid Earth 125(10):e2020JB020060. https://doi.org/10.1029/2020JB020060

Baba T, Cummins PR, Thio HK, Tsushima H (2009) Validation and joint inversion of teleseismic waveforms for earthquake source models using deep ocean bottom pressure records: a case study of the 2006 Kuril megathrust earthquake. Pure Appl Geophys 166(1–2):55–76. https://doi.org/10.1007/s00024-008-0438-1

Baba T, Takahashi N, Kaneda Y, Ando K, Matsuoka D, Kato T (2015) Parallel implementation of dispersive tsunami wave modeling with a nesting algorithm for the 2011 Tohoku tsunami. Pure Appl Geophys 172:3455–3472. https://doi.org/10.1007/s00024-015-1049-2

Bird P (2003) An updated digital model of plate boundaries. Geochem Geophys Geosyst. https://doi.org/10.1029/2001GC000252

Boston B, Moore GF, Nakamura Y, Kodaira S (2014) Outer-rise normal fault development and influence on near-trench décollement propagation along the Japan Trench, off Tohoku. Earth Planets Space 66(1):1–17. https://doi.org/10.1186/1880-5981-66-135

Chikasada N (2020) Global tsunami terrain model. https://doi.org/10.17598/NIED.0021

Fujie G, Kodaira S, Sato T, Takahashi T (2016) Along-trench variations in the seismic structure of the incoming Pacific plate at the outer rise of the northern Japan Trench. Geophys Res Lett 43(2):666–673. https://doi.org/10.1002/2015GL067363

Fujii Y, Satake K (2008) Tsunami sources of November 2006 and January 2007 great Kuril earthquakes. Bull Seismol Soc Am 98(3):1559–1571. https://doi.org/10.1785/0120070221

GEBCO Compilation Group (2019) GEBCO 2019 Grid. https://doi.org/10.5285/836f016a-33be-6ddc-e053-6c86abc0788e

GEBCO Compilation Group (2020) GEBCO 2020 Grid. https://doi.org/10.5285/a29c5465-b138-234d-e053-6c86abc040b9

Grilli ST, Tappin DR, Carey S, Watt SF, Ward SN, Grilli AR, Engwell SL, Zhang C, Kirby JT, Schambach L, Muin M (2019) Modelling of the tsunami from the December 22, 2018 lateral collapse of Anak Krakatau volcano in the Sunda Straits, Indonesia. Sci Rep 9(1):1–13. https://doi.org/10.1038/s41598-019-48327-6

Hamada N, Suzuki Y (2004) Re-examination of aftershocks of the 1952 Tokachi-oki earthquake and a comparison with those of the 2003 Tokachi-oki earthquake. Earth Planets Space 56(3):341–345. https://doi.org/10.1186/BF03353062

Headquarters for Earthquake Research Promotion (2018) Evaluations of occurrence potentials of subduction-zone earthquakes in the Kuril Trench, 3rd ed (**in Japanese**). https://www.jishin.go.jp/main/chousa/kaikou_pdf/chishima3.pdf

Ioki K, Tanioka Y (2016) Re-estimated fault model of the 17th century great earthquake off Hokkaido using tsunami deposit data. Earth Planet Sci Lett 433:133–138. https://doi.org/10.1016/j.epsl.2015.10.009

Izumi N, Nishizawa A, Horiuchi D, Kido Y, Goto H, Nakata T (2017) 3D bathymetric image of the southwestern part of the Kuril Trench and its vicinity. Rep Hydrogr Oceanogr Res 54:133–155 (**in Japanese with English abstract**)

Japan Coast Guard, JAMSTEC (2011) Bathymetry data off Tohoku, Japan. Seismol Soc Jpn News Lett 23(2):35–36 (**in Japanese**)

Japan Hydrographic Association (2009) D7006S-2 M7000 Digital Bathymetric Chart (Shapefile), Japan Hydrographic Association. https://www.jha.or.jp/shop/index.php?main_page=product_info_js2&products_id=1376. Accessed 01 Feb 2024

Japan Hydrographic Association (2011) J1508H JTOPO30v2-M1508, Japan Hydrographic Association. https://www.jha.or.jp/shop/index.php?main_page=product_info_js2&products_id=1274. Accessed 01 Feb 2024

Japan Hydrographic Association (2012) D7007S-2 M7000 Digital Bathymetric Chart (Shapefile), Japan Hydrographic Association. https://www.jha.or.jp/shop/index.php?main_page=product_info_js2&products_id=1378. Accessed 01 Feb 2024

Kajiura K (1963) The leading wave of a tsunami. Bull Earthq Res Inst 41:535–571

Kanamori H (1971) Seismological evidence for a lithospheric normal faulting—The Sanriku earthquake of 1933. Phys Earth Planet Int 4(4):289–300. https://doi.org/10.1016/0031-9201(71)90013-6

Kim S, Saito T, Kubota T, Chang S (2023) Joint inversion of ocean-bottom pressure and GNSS data from the 2003 Tokachi-oki earthquake. Earth Planets Space 75(1):1–15. https://doi.org/10.1186/s40623-023-01864-x

Kirby JT, Shi F, Nicolsky D, Misra S (2016) The 27 April 1975 Kitimat, British Columbia submarine landslide tsunami: a comparison of modeling approaches. Landslides 13:1421–1434. https://doi.org/10.1007/s10346-016-0682-x

Kobayashi K, Nakanishi M, Tamaki K, Ogawa Y (1998) Outer slope faulting associated with western Kuril and Japan trenches. Geophys J Int 134(2):356–372. https://doi.org/10.1046/j.1365-246x.1998.00569.x

Kubota T, Hino R, Inazu D, Suzuki S (2019) Fault model of the 2012Doublet earthquake, near the up-dip end of the 2011 Tohoku-Oki earthquake, based on a near-field tsunami: implications for intraplate stress state. Prog Earth Planet Sci 6(1):1–20. https://doi.org/10.1186/s40645-019-0313-y

Lay T, Ammon CJ, Kanamori H, Rivera L, Koper KD, Hutko AR (2010) The 2009 Samoa-Tonga great earthquake triggered doublet. Nature 466(7309):964–968. https://doi.org/10.1038/nature09214

Lay T, Kanamori H, Ammon CJ, Hutko AR, Furlong K, Rivera L (2009) The 2006–2007 Kuril Islands great earthquake sequence. J Geophys Res 114:B11308. https://doi.org/10.1029/2008JB006280

Ma G, Kirby JT, Hsu TJ, Shi F (2015) A two-layer granular landslide model for tsunami wave generation: theory and computation. Ocean Model 93:40–55. https://doi.org/10.1016/j.ocemod.2015.07.012

Ma G, Kirby JT, Shi F (2013) Numerical simulation of tsunami waves generated by deformable submarine landslides. Ocean Model 69:146–165. https://doi.org/10.1016/j.ocemod.2013.07.001

Ma G, Shi F, Kirby JT (2012) Shock-capturing non-hydrostatic model for fully dispersive surface wave processes. Ocean Model 43:22–35. https://doi.org/10.1016/j.ocemod.2011.12.002

Matsuda T (1990) Seismic zoning map of the Japanese Islands, with maximum magnitude derived from active fault data. Bull Earthq Res Inst 65:289–319

Baba *et al. Earth, Planets and Space*   (2024) 76:98

Page 14 of 14

Nakamura Y, Kodaira S, Miura S, Regalla C, Takahashi N (2013) High-resolution seismic imaging in the Japan Trench axis area off Miyagi, northeastern Japan. Geophys Res Lett 40(9):1713–1718. https://doi.org/10.1002/grl.50364

Nakanishi M (2011) Bending-related topographic structures of the subducting plate in the northwestern Pacific Ocean. In: Ogawa Y, Anma R, Dilek Y (eds) Accretionary prisms and convergent margin tectonics in the Northwest Pacific Basin. Springer, Dordrecht, pp 1–38. https://doi.org/10.1007/978-90-481-8885-7_1

Namegaya Y, Satake K (2014) Reexamination of the A.D. 869 Jogan earthquake size from tsunami deposit distribution, simulated flow depth, and velocity. Geophys Res Lett 41(7):2297–2303. https://doi.org/10.1002/2013GL058678

Nanayama F, Satake K, Furukawa R, Shimokawa K, Atwater BF, Shigeno K, Yamaki S (2003) Unusually large earthquakes inferred from tsunami deposits along the Kuril trench. Nature 424(6949):660–663. https://doi.org/10.1038/nature01864

Nishimura T (2009) Slip distribution of the 1973 Nemuro-oki earthquake estimated from the re-examined geodetic data. Earth Planets Space 61(11):1203–1214. https://doi.org/10.1186/BF03352973

Obana K, Fujie G, Takahashi T, Yamamoto Y, Nakamura Y, Kodaira S, Takahashi N, Kaneda Y, Shinohara M (2012) Normal-faulting earthquakes beneath the outer slope of the Japan Trench after the 2011 Tohoku earthquake: implications for the stress regime in the incoming Pacific plate. Geophys Res Lett 39:L00G24. https://doi.org/10.1029/2011GL050399

Obana K, Fujie G, Takahashi T, Yamamoto Y, Tonegawa T, Miura S, Kodaira S (2019) Seismic velocity structure and its implications for oceanic mantle hydration in the trench–outer rise of the Japan Trench. Geophys J Int 217:1629–1642. https://doi.org/10.1093/gji/ggz099

Obana K, Fujie G, Yamamoto Y, Kaiho Y, Nakamura Y, Miura S, Kodaira S (2021) Seismicity around the trench axis and outer-rise region of the southern Japan Trench, south of the main rupture area of the 2011 Tohoku-oki earthquake. Geophys J Int 226(1):131–145. https://doi.org/10.1093/gji/ggab093

Obana K, Nakamura Y, Fujie G, Kodaira S, Kaiho Y, Yamamoto Y, Miura S (2018) Seismicity in the source areas of the 1896 and 1933 Sanriku earthquakes and implications for large near-trench earthquake faults. Geophys J Int 212(3):2061–2072. https://doi.org/10.1093/gji/ggx532

Oishi Y, Piggott MD, Maeda T, Kramer SC, Collins GS, Tsushima H, Furumura T (2013) Three-dimensional tsunami propagation simulations using an unstructured mesh finite element model. J Geophys Res: Solid Earth 118(6):2998–3018. https://doi.org/10.1002/jgrb.50225

Okada Y (1985) Surface deformation due to shear and tensile faults in a half-space. Bull Seismol Soc Am 75:1435–1154. https://doi.org/10.1785/BSSA0750041135

Okal EA, Fritz HM, Synolakis CE, Borrero JC, Weiss R, Lynett PJ, Titov VV, Foteinis S, Jaffe BE, Liu PL-F, Chan I (2010) Field survey of the Samoa tsunami of 29 September 2009. Seismol Res Lett 81(4):577–591. https://doi.org/10.1785/gssrl.81.4.577

Peregrine H (1972) Equations for water waves and the approximations behind them. In: Meyer RE (ed) Waves on beaches and resulting sediment transport. Academic Press, New York, pp 95–121

Prabu P, Chaudhuri A, Bhallamudi SM, Sannasiraj K (2022) Three-dimensional numerical simulations for mitigation of tsunami wave impact using intermittent sea dikes. Ocean Eng 261:112112. https://doi.org/10.1016/j.oceaneng.2022.112112

Rubin CM, Horton BP, Sieh K, Pilarczyk JE, Daly P, Ismail N, Parnell AC (2017) Highly variable recurrence of tsunamis in the 7,400 years before the 2004 Indian Ocean tsunami. Nat Commun 8(1):1–12. https://doi.org/10.1038/ncomms16019

Saito T (2019) Tsunami generation and propagation. Springer Geophysics. https://doi.org/10.1007/978-4-431-56850-6_1

Satake K, Hirata K, Yamaki S, Tanioka Y (2006) Re-estimation of tsunami source of the 1952 Tokachi-oki earthquake. Earth Planets Space 58(5):535–542. https://doi.org/10.1186/BF03351951

Satake K, Nanayama F, Yamaki S (2008) Fault models of unusual tsunami in the 17th century along the Kuril trench. Earth Planets Space 60(9):925–935. https://doi.org/10.1186/BF03352848

Satake K, Nanayama F, Yamaki S, Tanioka Y, Hirata K (2005) Variability among tsunami sources in the 17th–21st centuries along the Soutehrn Kuril

Trench. In: Satake K (ed) Tsunamis. Adv Nat Tech Haz Res, 23. Springer, Dordrecht. https://doi.org/10.1007/1-4020-3331-1_9

Sandanbata O, Watada S, Ho T, Satake K (2021) Phase delay of short-period tsunamis in the density-stratified compressible ocean over the elastic Earth. Geophys J Int 226(3):1975–1985. https://doi.org/10.1093/gji/ggab192

Takeo M, Ide S, Yoshida Y (1993) The 1993 Kushiro-Oki, Japan, earthquake: a high stress-drop event in a subducting slab. Geophys Res Lett 20(23):2607–2610. https://doi.org/10.1029/93GL02864

Tanioka Y, Satake K (1996) Fault parameters of the 1896 Sanriku tsunami earthquake estimated from tsunami numerical modeling. Geophys Res Lett 23(13):1549–1552. https://doi.org/10.1029/96GL01479

Tanioka Y, Satake K, Hirata K (2007) Recurrence of recent large earthquakes along the southernmost Kurile-Kamchatka Subduction zone. Geophys Monogr 172:145–152

Tanioka Y, Nishimura Y, Hirakawa K et al (2004a) Tsunami run-up heights of the 2003 Tokachi-oki earthquake. Earth Planets Space 56(3):359–365. https://doi.org/10.1186/BF03353065

Tanioka Y, Hirata K, Hino R, Kanazawa T (2004b) Slip distribution of the 2003 Tokachi-oki earthquake estimated from tsunami waveform inversion. Earth Planets Space 56(3):373–376. https://doi.org/10.1186/BF03353067

Tanioka Y, Ramirez AGC, Yamanaka Y (2018) Simulation of a Dispersive Tsunami due to the 2016 El Salvador-Nicaragua Outer-Rise Earthquake (Mw 6.9). Pure Appl Geophys 175:1363–1370. https://doi.org/10.1007/s00024-018-1773-5

Tanioka Y, Ruff L, Satake K (1995) The great Kurile Earthquake of October 4, 1994 tore the slab. Geophys Res Lett 22(13):1661–1664. https://doi.org/10.1029/95GL01656

Tohoku University's School of Engineering & the Japan Nuclear Energy Safety Organization (JNES) (2010) Japan tsunami trace database. https://tsunami-db.irides.tohoku.ac.jp/tsunami/?LANG=-2. Accessed 15 March 2021

Tozer B, Sandwell DT, Smith WHF, Olson C, Beale JR, Wessel P (2019) Global bathymetry and topography at 15 arc seconds: SRTM15+. Earth Space Sci 6(10):1847–1864. https://doi.org/10.1029/2019EA000658

Tsuji H, Hatanaka Y, Sagiya T, Hashimoto M (1995) Coseismic crustal deformation from the 1994 Hokkaido-Toho-Oki Earthquake Monitored by a nationwide continuous GPS array in Japan. Geophys Res Lett 22(13):1669–1672. https://doi.org/10.1029/95GL01659

Wessel P (2019) GMT 5.4.5. https://github.com/GenericMappingTools/gmt/releases/tag/5.4.5

Yokoi H, Baba T, Lin Z, Minami T, Kamiya M, Naitoh A, Toh H (2023) Simultaneous inversion of ocean bottom pressure and electromagnetic tsunami records for the 2009 Samoa Earthquake. J Geophys Re: Solid Earth 128(6):e2023JB026956. https://doi.org/10.1029/2023JB026956

Publisher's Note